



Influence of Plastic Deformation and Hydroxyapatite Coating on Structure, Mechanical, Corrosion, Antibacterial and Cell Viability Properties of Zinc Based Biodegradable Alloys

B. Aksakal¹ · Ege Isin² · N. Aslan^{3,4} · S. Cihangir⁵ · S. Sezek⁶ · Yasemin Yilmazer⁷

Received: 15 February 2024 / Accepted: 29 April 2024 / Published online: 27 May 2024
© The Author(s) 2024, corrected publication 2024

Abstract

Zinc (Zn)-based biodegradable alloys have been at the forefront of absorbable biomaterial research in recent years due to their high biocompatibility and corrosion rates. The arc melting process was used to produce the Zn–1Cu–1Ag biodegradable alloy. The influence of different plastic deformation rates on the microstructure of the material was examined after the cold rolling at deformation rates of 47% and 61%. The undeformed and deformed alloys have been hydroxyapatite-coated using the electrophoretic deposition process to improve its surface, corrosion, and bioactivity properties. Optical, XRD, SEM, and EDS examinations were used to analyze the samples' uncoated, coated, and rolled-unrolled forms. The nucleation of the (Ag, Cu)Zn₄ secondary phase was formed during the rolling process. Hardness and compression tests were used to determine the mechanical properties of cast and rolled alloys, and in vitro corrosion tests were carried out in simulated body fluid. Antimicrobial and cell viability tests are executed to demonstrate the biocompatibility of the deformed and HA-coated Zn–1Cu–1Ag alloy. The mechanical properties were improved after the rolling process, with the highest results found in 47% of the rolled samples exhibiting a compressive strength of 412.65 ± 0.5 MPa and 61% of the rolled samples exhibiting a hardness value of 88.1 ± 0.5 HV. The samples that were rolled (61%) and coated with hydroxyapatite (HA) exhibited the highest level of corrosion resistance. The antimicrobial tests revealed that the rolled and HA coated Zn1Cu1Ag groups exhibited greater inhibition rates (47 and 61%) compared to the other groups when tested against *E. coli*. The HA-coated groups exhibited good cell viability ratios, with the maximum viability seen in the rolled and HA-coated group at 47%.

Keywords Biodegradable metals · Zn–1Cu1Ag · Rolling · EPD coating · Corrosion · Cell viability

1 Introduction

Natural or synthetic biodegradable materials used to fulfill or sustain the functions of live tissues in the human body, which are necessary when tissues or organs in the human body lose function for a number of causes [1]. The term "biodegradable metals" refers to materials that completely degrade in the body due to the physiological environment in which they are retained while also promoting tissue healing as they do so [2]. Such metals, after they have served their purpose, totally breakdown within the body, leaving no harmful residues behind or having an unfavorable effect on the immune system. This eliminates the requirement for further surgery to remove the toxic effect it has on the body [3].

Permanent implants are normally removed when the healing process is completed to avoid any side effects necessitate a second surgery [4]. The new biodegradable biomaterials help the healing process and ultimately dissolve as a result

✉ B. Aksakal
baksakal@firat.edu.tr

¹ School of Civil Aviation, Department of Aircraft Fuselage Engine, Firat University, Elazig, Turkey

² Graduate School of Science and Engineering, Yildiz Technical University, Istanbul, Turkey

³ Department of Metallurgical and Materials Engineering, Munzur University, Tunceli, Turkey

⁴ Rare Earth Elements Application and Research Center, Munzur University, Tunceli, Turkey

⁵ Department of Chemistry and Chemical Processes, Tunceli Vocational School, Munzur University, Tunceli, Turkey

⁶ Engineering Faculty, Department of Mechanical Engineering, Atatürk University, Erzurum, Turkey

⁷ Department of Molecular Biology and Genetics, Sabahattin Zaim University, Istanbul, Turkey

of the physiological environment inside the body, eliminating long-term negative effects without the need for surgical removal [5]. Biodegradable metals are classified into three major categories: iron (Fe), magnesium (Mg), and zinc (Zn); however, despite extensive research into Fe and Mg, Zn research has just recently begun [6]. Zn serves as a necessary basic element for the body and is involved in several biological processes, including DNA synthesis and nucleic acid metabolism [7]. In a study by Bowen et al. [8] on pure Zn wire in rat abdominal aorta, it was discovered that Zn had excellent biocompatibility and better corrosion behavior. Although it is regarded as one of the best candidates among biodegradable metals, investigations to improve the mechanical and biocompatibility of Zn-based products have been the main emphasis in recent years [6]. According to a prior study, zinc's mechanical and corrosion properties were greatly improved by elemental supplements such as calcium, magnesium, strontium, aluminum, lithium, copper, and silver [9]. It was reported that Cu supplementation enhances the mechanical properties of Zn, such as the operations such as rolling and extrusion. However, the effect of Zn on corrosion behavior is unknown [10–14], because Cu is also a trace element that is essential for human health and serves as a cofactor for various enzymes. In this context, Zinc alloy solutions for use in load-bearing applications have been developed by Yang et al. [9]. The investigation involved alloying and extruding Zn with the comparatively high solubility elements Ca, Fe, Sr, Mg, Li, Mn, and Cu, as well as Ag. Zn–*x*Cu (*x* = 1, 2, 3, 4%, respectively) alloys' microstructure and mechanical characteristics were investigated by Tang et al. [12]. They concluded that the microstructures are Zn matrix and CuZn₅, except for Zn–1Cu, based on their optical microscope and XRD analyses.

When similar studies were evaluated, it was seen that Cu supplementation did not influence the corrosion rate [10]. Furthermore, due to its antibacterial qualities, silver has been used for many years in biomedical applications such as burn and wound treatments [15]. Previous studies have indicated that alloying Zn with Ag enhances the mechanical properties and corrosion rate [16]. However, the number of studies involving Cu and Ag alloying is fairly limited, and the effect on microstructure, mechanical, and corrosion properties remains an important research topic. Jasinska et al. [15] produced Zn–*x*Cu (*x* = 2.5%, 5%, 7.5%) alloy and it was found that the corrosion rate increased with Ag concentration in the immersion tests performed following the extraction process. Because biocompatibility is crucial for life body, biomaterials should be unaffected by physiological fluids, undistorted, and non-corrosive. Such features must be sufficient and similar to those of bone, have appropriate weight and density values, do not generate reactions other than those that occur naturally in the body, and are acceptable to the host tissue [17].

Hydroxyapatite (HA) is being used with various coating methods to improve the biodegradation time of traditional bioinert metals with its osteoconductivity properties and to prevent implant wear by providing bond formation between the host tissue and the implant due to its excellent bioactivity, high biocompatibility, and excellent osteoconductivity [18, 19]. Many coating processes have been utilized to prepare HA coatings, including plasma spraying [20], sol–gel [21–23], hydrothermal [24, 25], and electrophoretic deposition [18, 26, 27]. The interest in the electrophoretic deposition method (EPD) to produce HA coatings is based on factors such as good stoichiometry control, easy and quick deposition at room temperature, high purity of the material to be coated on the substrate surface that is difficult to obtain using other techniques, and the ability to deposition on complex-shaped substrates [28, 29]. Although Zn corrodes at a slower rate than the other biodegradable metals like magnesium and iron, its corrosion behavior may need to be modified to create a balance between bone growth and metal breakdown. The reinforcement and mechanical treatments affect the corrosion behavior of such alloys while also increasing its mechanical qualities [30].

While the majority of research on Zn-based biodegradable materials has concentrated on the alloying impact, no investigations on the deformation effect or bioactive properties using Zn–Cu–Ag triple alloy coating have been undertaken concurrently in the literature. In this study, the biodegradable Zn–1Cu–1Ag alloy was created, deformed with different rolling ratios, and coated utilizing the EPD technique. Mechanical properties, as well as corrosion resistance and biocompatibility, were evaluated using morphological alterations.

2 Materials and Method

2.1 Material Production

In this work, 99.9% pure zinc (Zn), copper (Cu), and silver (Zinc shot, 10 mm dia x 2 mm thick, 99.99% (Alfa Easer, 10,440.36), Silver nitrate, RPE-ACS, (Carlo Erba, CE.423954), Copper shot, 1–10 mm, 99.9% (Alfa Easer, 10159.36) particles were used as the individual biodegradable components. Cu and Ag grains range in size, but Zn grains are the same size, therefore particular care was taken to ensure that they were small and homogeneous. This facilitated consistent distribution and lowered the possibility of grain melting during casting. Before casting, 5 × 200 g Zn–1Cu–1Ag packs (98 wt% Zn, 1 wt% Cu, 1 wt% Ag) were made available. The scaling was taken using a precision balance (Thermo Scientific-Orion A111) and then packaged separately.

To avoid temperature variations, the graphite crucible to be cast was placed in a vacuum furnace (Thermonevo, Turkey) during heating. To ensure a uniform distribution, 50% of the Zn was manually poured into the crucible, followed by the remaining 50% of zinc, as well as any available copper and silver. The filled crucible was transferred into the furnace with tongs, and the time of putting the crucible into the furnace was recorded after vacuuming. Three stirs with a graphite rod were performed every half hour to ensure a homogenous casting. Following the final stirring, the crucible was returned to the furnace for another 15 min, and the alloy melt was poured into the 11.2 × 11.2 × 110 mm steel mold before being returned to the furnace. After the mold had cooled for about 10 min, two 100-g samples were obtained, totaling ten samples. The crucible was removed from the furnace following the initial casting procedure, and two samples were placed inside. The stages of the second casting process were identical to those of the first. The main distinction is that the casting mold is heated to around 250 °C to ensure homogeneity and more controlled cooling. After casting, the mold was unplugged from the power source and allowed to cool at ambient temperature. Due to the mold's elevated temperature, the samples were extracted while wearing protective gloves and subsequently transferred to a homogenization furnace. Homogenization was employed to ensure that Zn, Cu, and Ag were distributed uniformly throughout the structure. The process was carried out in the homogenization furnace (Vulcan 3–550) for 16 h at 350 °C. After the process, the samples were removed from the furnace and quenched to cool. Before the rolling process, the quenched samples were cleaned with ethanol. The structural inconsistencies that arose during the solidification process were resolved, leading to a uniform dispersion of Zn, Cu, and Ag.

2.2 Rolling Process

A dual rolling system was employed, utilizing rolls with a diameter of 200 mm and the rotation rate of 50 rpm. The deformation ratios have been kept constant, and the samples undergone deformation at deformation ratios of 47% and 61% in order to assess the potential shape alteration that may occur in each sample throughout the rolling process. Because surface porosities could interfere with the cutting process, the rolled samples were surface polished with sandpaper before being cut. A wire erosion machine (Charmilles Technologies ARVEN Makine-Robofil 510) was used to cut rolled plates. Samples were obtained on a counter using the wire erosion process, where an electric current was applied to a wire that was stretched vertically.

2.3 Metallography

The procedure of abrasive sandpapering was carried out using a manual abrasive sandpapering machine operating at a speed of 200 rpm. The sandpapers utilized had mesh sizes ranging from 120 to 2500 silicon carbide sandpapers. After the sandpapering process, the samples were subjected to cleaning using 96% pure ethyl alcohol. The three samples, which were unrolled, 47% rolled, and 61% rolled, were subjected to electrolytic polishing at a rate of 0.1 V/2 s. The polishing procedure was conducted utilizing a power source, employing a 50 ml solution of 99.9% pure ethyl alcohol and an equal volume of phosphoric acid solution. The samples underwent a cleaning process using alcohol and were subsequently dried at ambient temperature. Following this, they were immersed in the same solution for a duration of 3 s, after which they were etched and washed with tap water.

2.4 Electrophoretic Deposition (EPD) Process

Following metallographic preparation and rolling of the Zn–1Cu–1Ag alloys at 47% and 61% ratios, a HA coating process was applied to improve surface properties. The assembly for performing EPD was equipped with a DC power supply. A stainless-steel plate was used to place the samples in the anode and countering cathode respectively. The EPD method was optimized using process parameters of 60, 90, and 120 V and deposition periods of 5, 10, or 20 s, with a fixed electrode distance of 10 mm. After optimization, the EPD coating technique [18] for all samples was performed at 5 s and 60 V using a DC power source to distribute HA in distilled water (DW) containing iodine. The coated samples were dried for 24 h at room temperature before being dried for another 2 h in an oven at a temperature of 130 °C. Finally, the coated samples were sintered at 350 °C for 2 h in a vacuum with Ar flow. After sintering, all samples were placed in a desiccator to be characterized, analyzed, and tested.

2.5 Structural Characterization

Following the standard metallographic procedures, the microstructures generated in the as-cast and rolled Zn–1Cu–1Ag were examined at various magnifications with a Nikon Inverted Optical Microscope (Eclipse MA 100) to determine the effect of the rolling process on microstructures. The current phases of the as-cast, 47%, and 61% rolled samples were examined using XRD analysis. This analysis was carried out using a Rigaku Miniflex-600 at a wavelength of 1.5406 (k) with a step rate of 0.002° between 30° and 80°. For the SEM and EDS investigations, a Hitachi/SU3500 scanning electron microscope and an Oxford INCA X-ray spectrometer were used.

2.6 Mechanical Tests

The hardness test is often used to determine mechanical properties due to its simplicity, speed and low cost. A Vickers Hardness Tester (Mitutoyo HM-112, Japan) was used to determine hardness values at 0.2kgf (1.96 N) load. The standard deviation was calculated by collecting measurements at four separate spots on the sample and estimating the mean. Compression tests (Shimadzu-100 kN, Japan) are performed to demonstrate the strength of Zn-based alloys.

2.7 Wettability Tests

The wettability of the material surfaces is critical in determining the coating's adherence quality to the material surface. Wettability analysis was performed on Biolin Scientific brand Attension Theta Flex model Complete Range of Optical Tensiometers to analyze the hydrophilic and hydrophobic qualities of the material's surface. The tests were performed at a maximum measurement speed of 3009 fps, with a measurement precision of 0.1o and a surface tension measurement sensitivity of 0.001 mN/m. 5 μ l of water were dropped on the sample surface, and 14 photos were taken every 10 s.

2.8 In Vitro Corrosion Tests

The in vitro corrosion behaviors of the uncoated and HA-coated Zn–1Cu–1Ag alloys were examined using a potentiostat/galvanostat (Gamry, 1010E) device. Electrochemical measurements in simulated body fluid (SBF) at 36.5 °C were carried out by the potentiodynamic scan (PDS). Ag/AgCl and 25 cm² Pt were used as reference and counter electrodes, and produced alloys served as working electrodes. SBF was prepared by commonly applied procedures in the literature [31], using the reactives stated in Table 1. The scanning window was decided as 350 mV due to emerging noise for the wider potential window applications. In the experimental procedure, the 0.2 mV s⁻¹ scan rate was applied from –150 mV of open circuit potential (OCP) to 100 mV of OCP. The scan rate was kept low for the reasonable application of the Tafel technique. From the obtained anodic and cathodic curves, corrosion current and corrosion rate values were calculated via the Tafel extrapolation method.

2.9 Antibacterial Analysis

The disc diffusion test was used to evaluate the antibacterial activity of the alloys [32]. *E. coli* (ATCC 25922) suspensions were adjusted to 0.5 McFarland standard density from 18-h nutritional broth cultures to achieve a suitable bacterial density (1.5×10^8 CFU mL⁻¹). Mueller–Hinton agar plates were inoculated with 0.1 ml of the bacterial suspensions. After being rinsed in an ultrasonic bath with water and ethyl alcohol for 3 min, the samples were sterilized for 30 min under UV radiation with a wavelength of 254 nm. The test samples were prepared and then put on Petri dishes with bacterium plates. After 24 h of incubation at 37 °C, the inhibition zone surrounding the discs was measured using a digital micrometer [33]. To choose the best samples several groups have been formed, and tests were carried out three times.

2.9.1 Cell Viability Analysis

The cytotoxicity experiment was performed using the L929 mouse fibroblast cell line according to the UNI EN ISO 10993 regulation [34]. The cell lines were maintained in DMEM/F12 media supplemented with 10% fetal bovine serum and 1% penicillin/streptomycin at 37 °C and 5% CO₂. Trypsinization was carried out to remove confluent cells from the surface, and a hemocytometer was used to count the number of cells in the pellet after centrifuging the cells. The cells were then subsequently subjected to cytotoxicity tests. The L929 cells were cultured on 96-well plates, with each well containing 10³ cells and the produced samples were then placed in the cell culture medium for cytotoxicity assays and image analysis. The plates were subsequently incubated at 37 °C for durations of 24, 48, and 72 h. The cytotoxic effect was determined using the MTT (3-(4,5-dimethylthiazol-2-yl)-2,5-diphenyltetrazolium bromide) technique [35] The cell culture medium was replaced with 100 μ l fresh medium and 15 μ l of MTT solutions and incubated for 2 h in the dark. After incubation, the absorbance values of the wells were calculated using a micro-plate reader and a reading at 570 nm. Each assay was repeated five times. A sample is defined as cytotoxic if the percentage vitality value is 70% or below, and noncytotoxic if the percentage vitality value is greater than 70%(5). After 24 h of incubation, the materials applied L929 fibroblast cell images were observed in an inverted microscope (Leica DMI6000).

Table 1 Simulated body fluid (SBF) solution

NaCl (g \times L ⁻¹)	NaHCO ₃	KCl	K ₂ HPO ₄ •3H ₂ O	MgCl ₂ •6H ₂ O	c(HCl)	CaCl ₂	Na ₂ SO ₄	TRIS	c(HCl)
8.035	0.355	0.225	0.231	0.311	39 ml	0.292	0.072	6.118	0–5 ml

2.9.2 Statistical Analysis

The samples were analyzed with a one-way ANOVA test and independent-sample t-tests were used to describe significant differences between samples. Results were presented as mean \pm standard deviation. The level of significance was selected as $p < 0.05$.

3 Results and Discussion

3.1 Microstructure and XRD Analyses of Uncoated Samples

Secondary phases are formed as a result of peritectic transformation in both alloy systems, specifically the Zn–Cu and Zn–Ag binary alloys. These phases are known as (Cu, Zn)₄ and (Ag, Zn)₃, respectively, in the hexagonal closed-packed (HCP) structure, which is extremely comparable to the lattice structure of the zinc matrix [36]. Considering the alloys created, it is anticipated that the peritectic transformation will lead to the development of the HCP-structured (Ag, Cu)Zn₄ phase in accordance with the Zn–Cu–Ag ternary phase diagram [37]. As-cast, 47%, and 61% rolled samples underwent XRD and SEM–EDS studies to determine the overall microstructure and the presence of phases.

No secondary phase peaks were detected in the as-cast sample of the Zn–1Cu–1Ag alloy, according to the XRD spectra shown in Fig. 1, although minor secondary phase peaks appeared when the rolling ratio increased. Such phenomenon has also been observed in previous studies, wherein it has been determined that the influence of plastic deformation leads to the emergence of secondary phase

peaks, even when the alloying element level is modest [38]. This can be explained by the low recrystallization temperature of zinc, which allows secondary phase particles to develop by dynamic recrystallization of the samples even at room temperature [39]. According to the spectra, secondary phase formations of (Ag, Cu)Zn₄ are seen in 47% and 61% of rolled samples, but no intermetallic phase formation is seen in the cast sample. The formation of the (Ag, Cu)Zn₄ intermetallic phase was also observed when utilizing the ternary alloy system [38]. Although intermetallic phase formation is observed in 47% of rolled samples, less than 61% of rolled samples exhibit it. Because such peaks are relatively small, it may be concluded that intermetallic phase formation increases as rolling rate increases. When the graph is analysed, it is seen that phase peaks appear, as does the difference between the as-cast sample and the sample with an intermetallic phase.

Figure 2a shows the optical microscope images of the casting Zn1Cu1Ag samples. Upon analysis of these photographs, it becomes evident that a structure with a single phase and coarse grains is formed. The microstructure image encircles the resultant faults in order to accentuate their presence. Based on previous academic studies, it has been noticed when plastic deformation is applied to the alloy, it is anticipated that the grains will exhibit gravitational forces in the same direction [40, 41].

Figure 2a illustrates that the grains experienced deformation and elongation, resulting in a rolling effect of 47%. The observed phenomenon of grain thinning and increased orientation in the rolling direction suggests the potential occurrence of secondary phase formation, as indicated by the X-ray diffraction (XRD) peaks. Upon inspection of the optical microscope image, it becomes evident that the grains encompassing the white grains, as shown by the arrow, exhibit a lower size compared to the surrounding structures. Another observation made in a previous study [41] was that the size of the grains decreased in regions where there was a significant precipitation of secondary phase particles. Based on the available evidence, it can be inferred that the formation of these white deposits can be attributed to the precipitation of the secondary phase (Ag, Cu)Zn₄.

In certain regions of the 61% rolled samples (Fig. 2d, e), the grains exhibit elongation, while in other regions, the presence of micro equiaxed grains is observed. Deformation leads the grains to become smaller and fracture, causing them to move in the direction of rolling. Moreover, it was shown that the (Ag, Cu)Zn₄ phase is present at submicron sizes [41]. Consequently, distinct white precipitates were formed in various regions of the optical microscope images, despite the absence of secondary phases exhibiting dendritic patterns. Upon considering these precipitates, it becomes evident that the grains in close range to the white precipitations have a lower size compared to the other grains.

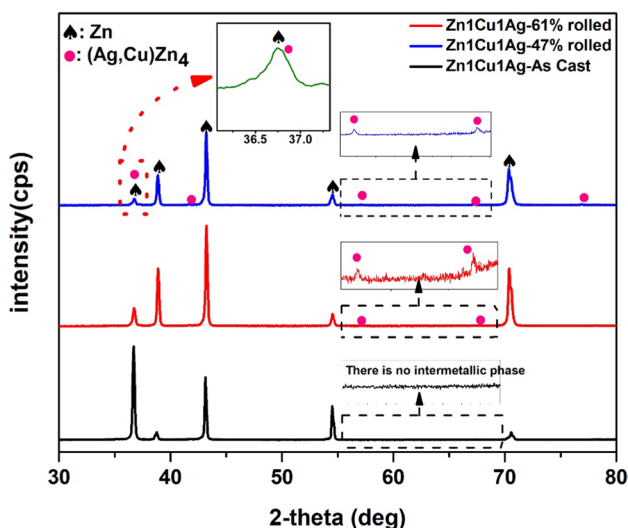
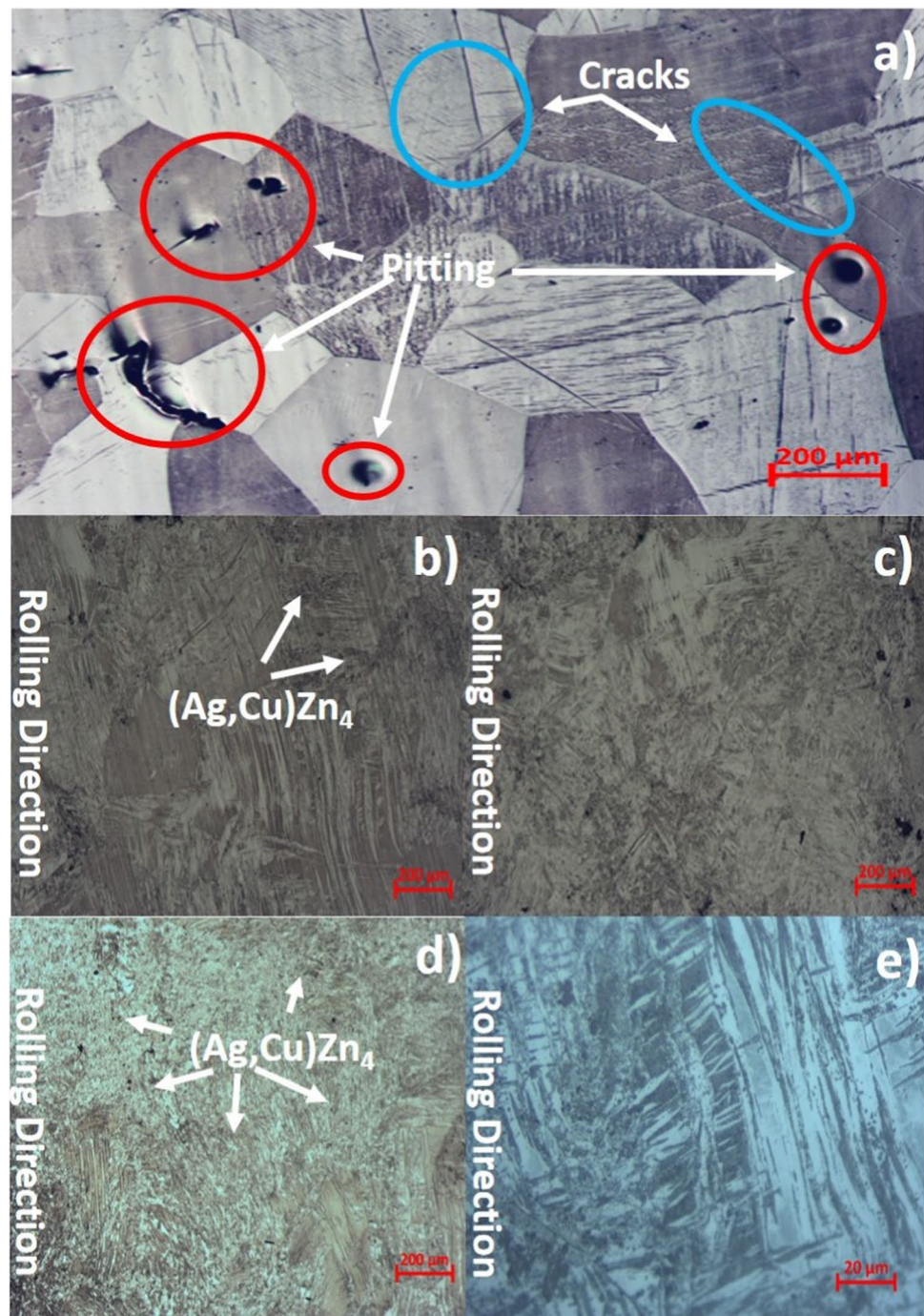


Fig. 1 XRD plots of as-cast, 47%, and 61% rolled Zn1Cu1Ag samples

Fig. 2 The optical images of the as-cast **a**, 47% rolled samples **b**, **c** and 61% rolled samples **d**, **e**



It is noteworthy that very small and equiaxed structures are formed as shown in Fig. 2b and Fig. 2d. The formation of such a structure can be attributed to Zn's low recrystallization temperature and dynamic recrystallization at high deformation rates. When these two structures are compared, it can be concluded that the secondary phase particles precipitated increase with increasing deformation, as supported by the XRD graphs.

Twinning formations in the microstructure occurred as a result of plastic deformation in 47% and 61% of rolled

samples, respectively. When Fig. 2c is examined, it is clear that the grains are stretched along the rolling direction, as shown in the preceding photos, and distortions arise due to the deformation effect. Twinning is represented by the red structures, while the blue-ringed areas are polishing deposits. As shown in Fig. 2e, samples exposed to 61% rolling processing produced the same shaped microstructures. SEM images and EDS-mapping analysis of uncoated cast, 47% and 61% rolled Zn1Cu1Ag samples are shown in Fig. 3. When comparing the samples depicted

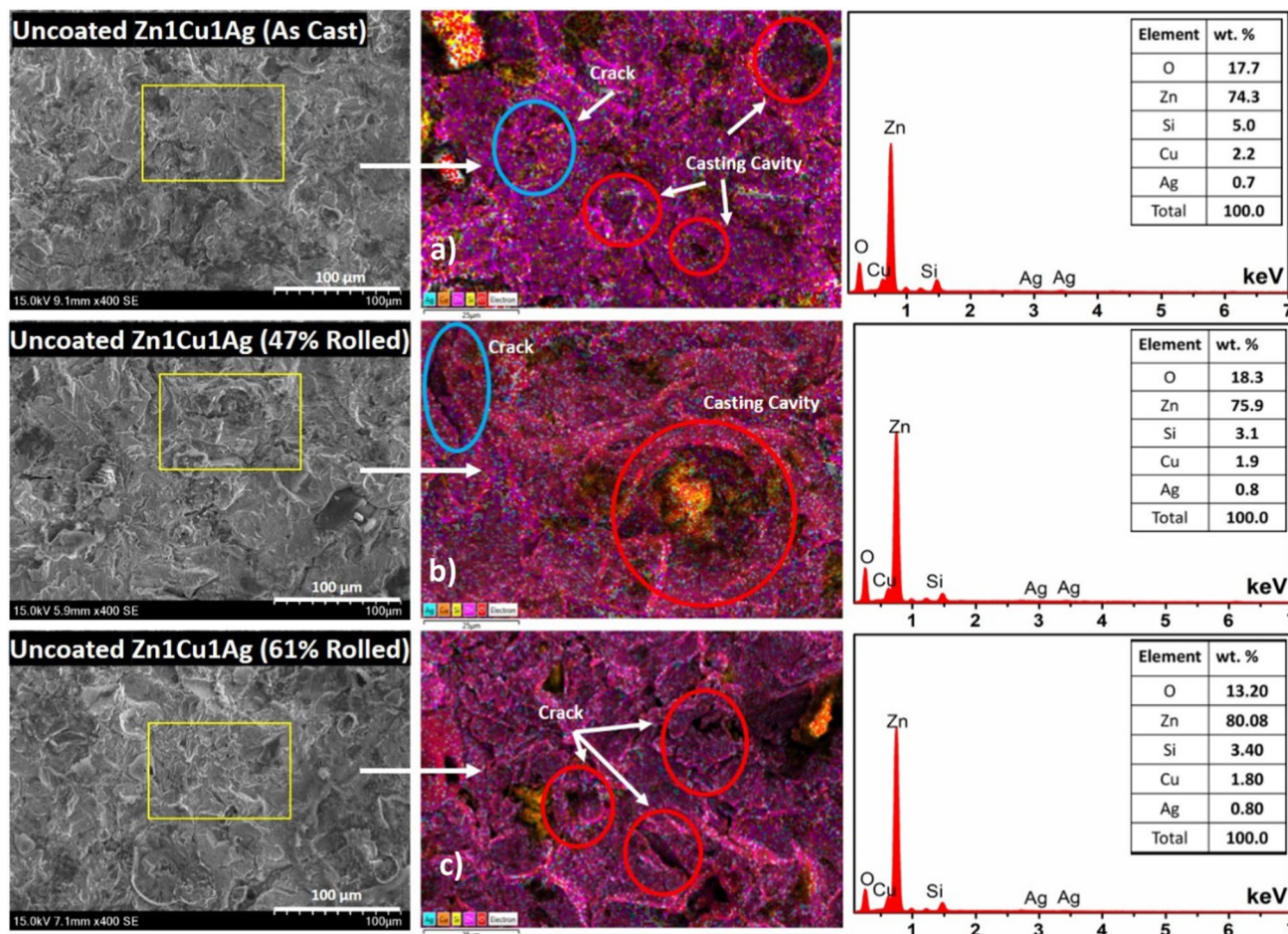


Fig. 3 SEM images and EDS-mapping analysis of **a** uncoated as-cast, **b** 47%, and **c** 61% rolled samples

in Fig. 2b–e, which underwent rolling at 47% and 61% respectively, to the as-cast sample, it becomes evident that the grains exhibit a significant increase in fineness, torsion, and alignment in the rolling direction.

Upon analysis of the images, it became evident that the grain boundaries, surface imperfections, casting voids, and cracks were readily apparent. White components can be seen in regions that are thought to be casting voids when the EDS analysis images are examined. The colored elemental distribution maps and EDS spectra that were acquired after EDS analysis. These maps allowed for the detection of Si and Oxygen-O as well as the expected elements of Zn, Cu, and Ag. It is likely that variations in wt% results were driven by factors such as Zn evaporation during casting and secondary phase development happening more frequently in particular places despite homogeneous conditions. Furthermore, O was detected as a result of the casting voids, and Silisium (Si), which had accumulated on the surface during the polishing step, was observed in the integrated white areas seen in the EDS spectrum.

3.2 Morpho-Structural Analysis of HA Coated Samples

The sample coating thicknesses were measured using SEM to ascertain the average coating thickness and coating topography. The results of the examinations indicated that the mean thickness of the coating was 42.5 μm . Furthermore, it was observed that achieving uniform coating coverage throughout the entire surface posed challenges. Figure 4 depicts an image illustrating the thickness of a coating.

In Fig. 5, SEM images and EDS spectra obtained after HA-coating of as-cast, 47% rolled and 61% rolled samples are given. The analysis of SEM pictures and EDS elemental mapping revealed the absence of a homogeneous coating and the presence of localized fissures. The purple portions of the photos correspond to structures with a Zn weight. The presence of Ag, Cu, and Si was also detected in locations abundant in zinc. The remaining components of the HA structure exhibit the presence of calcium (Ca), phosphorus (P), and oxygen (O). Upon examination of these photos, it becomes

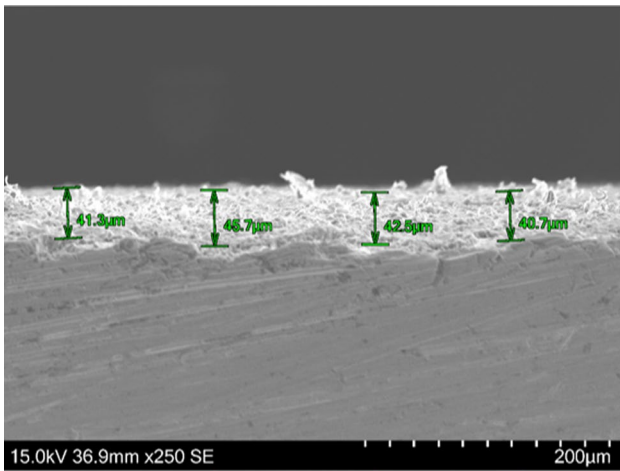


Fig. 4 HA-Coating film thickness on Zn1Cu1Ag alloy

evident that a uniform coating is not achieved, as it has a coarse structure and lacks strong adhesion to the surface.

Figure 6 shows the diffraction patterns of HA-coated cast, 47% and 61% rolled Zn1Cu1Ag samples. Upon examination of the X-ray diffraction (XRD) graphs, it becomes evident that the alloy system exhibits peaks corresponding to the Zn, Ag, and Cu elements, in addition to the peaks associated with the hydroxyapatite (HA) structure on the surface.

3.3 Mechanical Tests

The graph in Fig. 7 illustrates the values obtained from the microhardness and compression tests. The average hardness was determined by performing repeated tests on four separate measurements for each sample. The hardness values of the as-cast, 47%, and 61% rolled samples are 88.1 ± 3.02 , 73.7 ± 1.8 , and 88.1 ± 0.5 HV, respectively. The hardness values indicate the impact of grain refinement on the samples following the rolling process. Based on the findings, the highest recorded hardness value was observed in a specimen

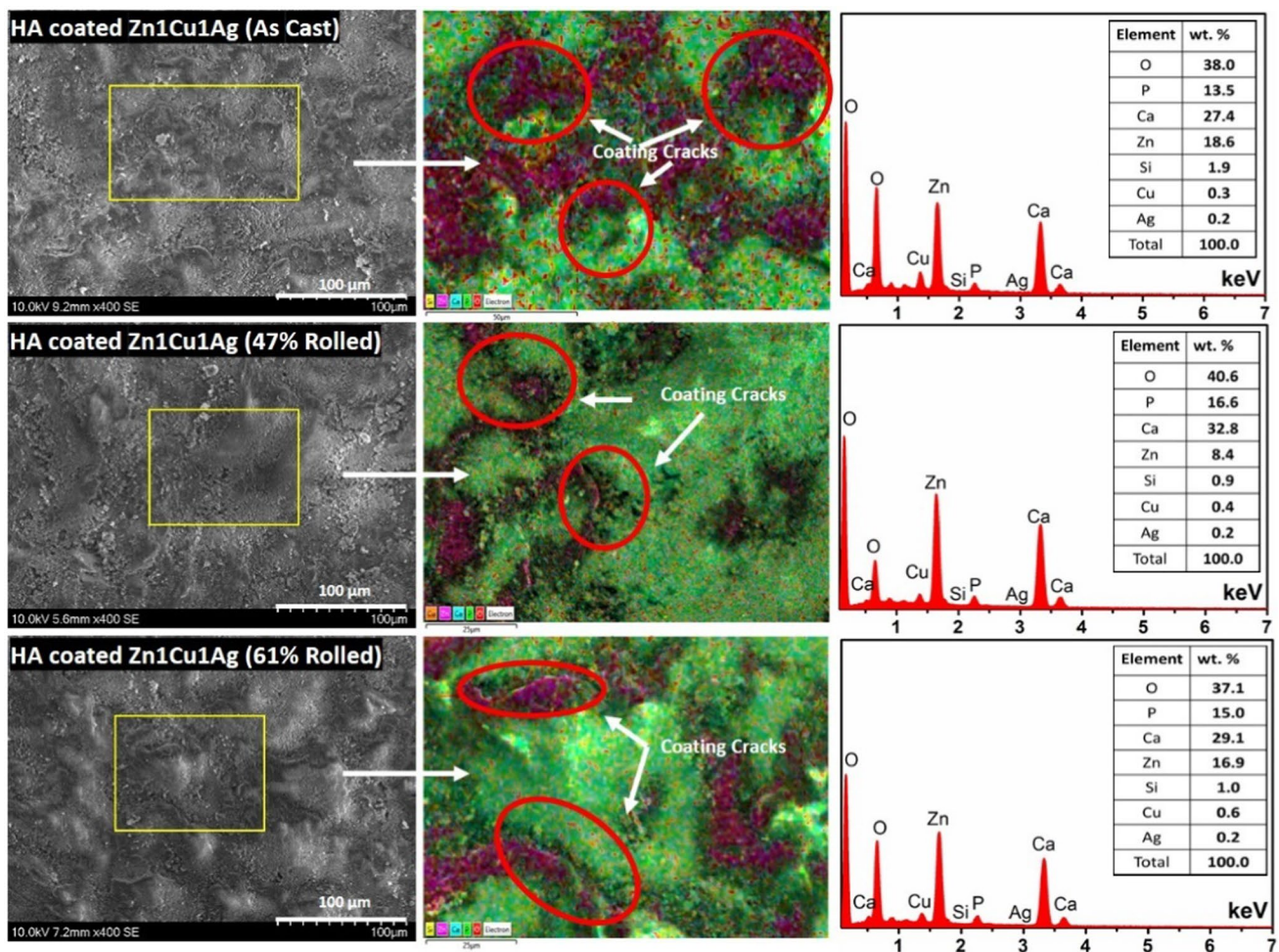


Fig. 5 SEM images and EDS-mapping analysis of a HA coated as-cast, b 47%, and c 61% rolled samples

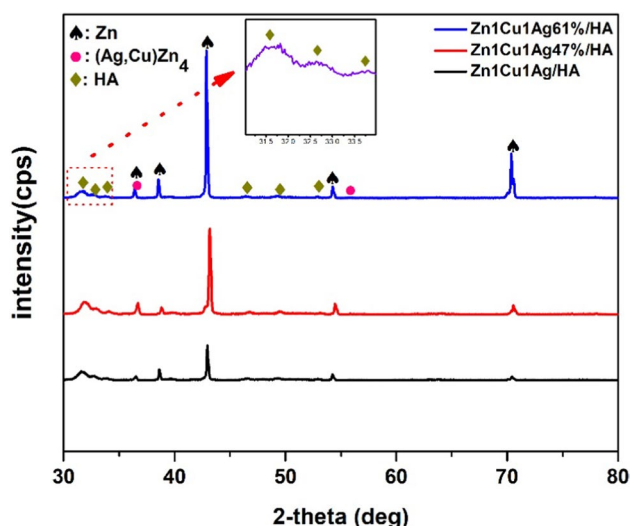


Fig. 6 XRD patterns of HA-coated cast, 47% and 61% rolled Zn1Cu1Ag samples

that experienced 61% rolling, resulting in a hardness value of 88.2 HV. The hardness value of the 47% rolled sample (73.7 HV) is higher than that of the as-cast sample, however the increase is smaller compared to the 61% rolled sample.

According to the compression test findings on the as-cast and rolled samples, the maximum compression strength (412.6 MPa) was found for the 47% rolled samples. The 61% rolled samples are expected to have better strength, yet the results for these samples are the lowest. This is because high deformation rates cause distortions in Zn and the CuZn5 solid solution phases [42] distributes more along grain boundaries with considerable cold deformation thus decreasing the mechanical properties. Upon examining the optical

and scanning electron microscopy (SEM) images of the cold rolled biodegradable Zn1Cu1Ag alloy at various rates, it was observed that specific micron-sized constituents were distributed along the grain boundaries of the precipitate, while others were disseminated within the grains (Figs. 2 and 3). The alloy structure displayed fractures, crushing, and grain elongation along the rolling direction due to substantial plastic deformation of the CuZn5 particles.

3.4 Wettability Analyzes

The wettability analysis findings are presented in Fig. 8. The as-cast, 47% rolled, and 61% rolled samples exhibit wettability values of 102.3°, 110.6°, and 104.08°, respectively. The magnitude of the contact angle between the liquid and the solid surface depends on the distribution of the liquid on the solid surface. The more undispersed the liquid remains, the larger the angle will be. If the angle is less than 90°, it is decided that it wets the solid surface; if it is larger than 90°, partial wetting occurs; and if it is greater than 140°, it demonstrates strong non-wetting capabilities [43]. Examining the data revealed that the cohesion strength was greater than the adhesion strength and had a slightly hydrophilic property, implying that a flawless, completely smooth coating cannot be emerged.

3.5 In vitro Corrosion Tests

The corrosion behavior of coated and uncoated samples has been examined in simulated bodily fluid (SBF). Tafel curves were obtained following the potentiodynamic measurements, shown in Fig. 9, and corrosion parameters (I_{corr} , E_{corr} , a ,

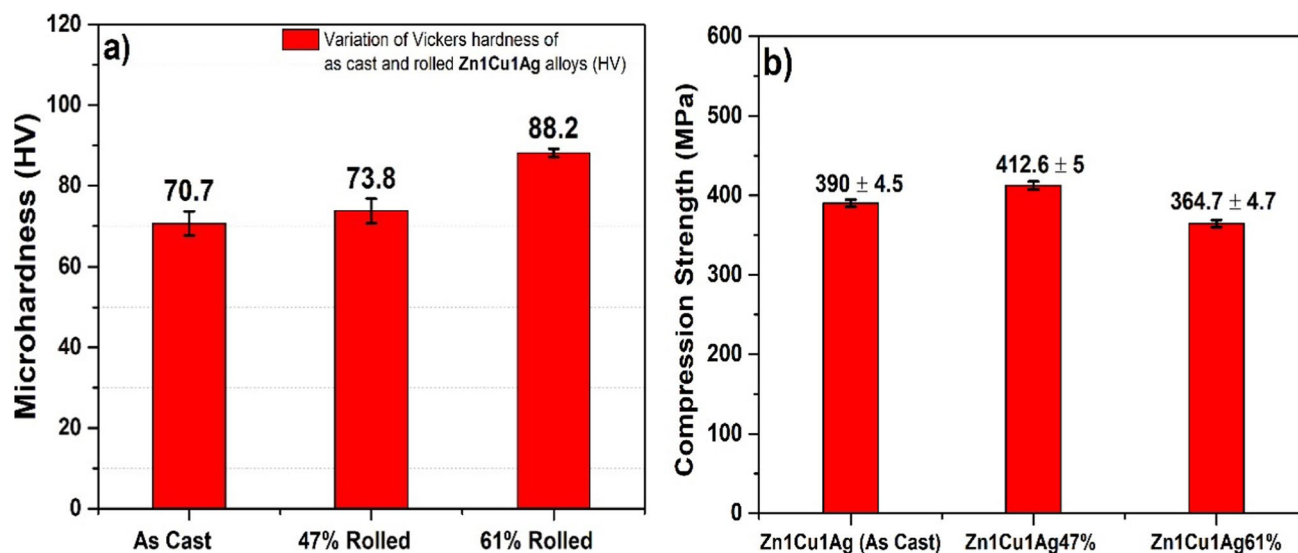


Fig. 7 Microhardness **a** and compression **b** values obtained for as cast, and rolled Zn1Cu1Ag samples

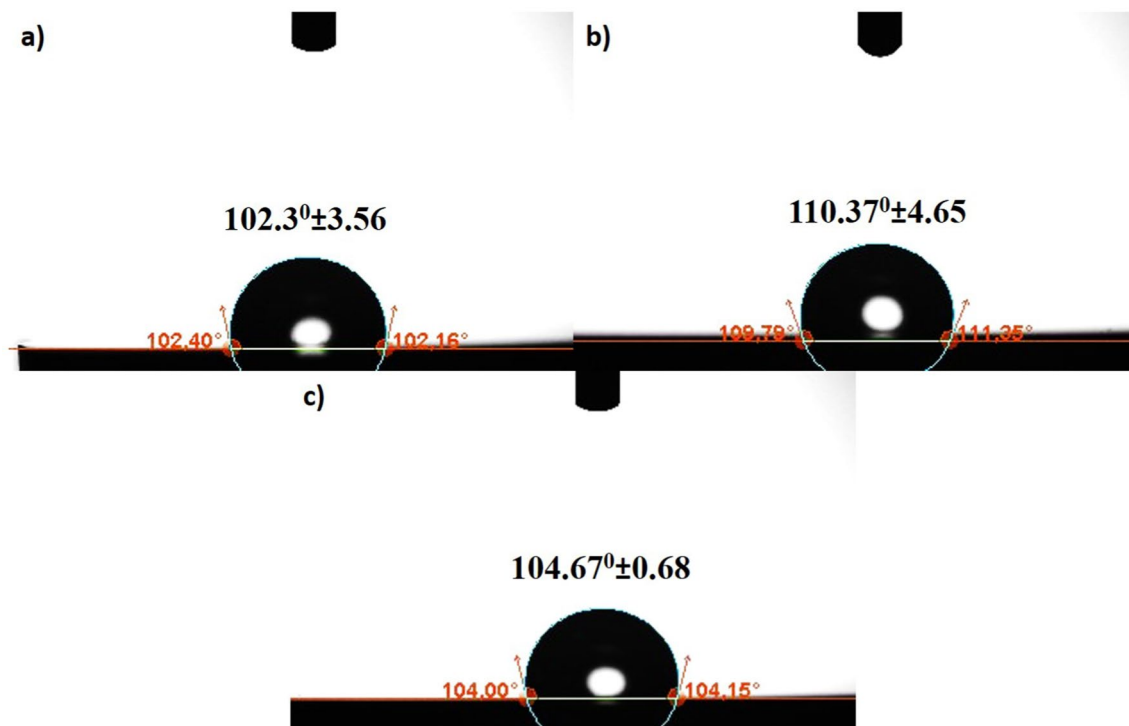


Fig. 8 Wettability analyzes **a** as-cast, **b** 47% rolled, **c** 61% rolled samples

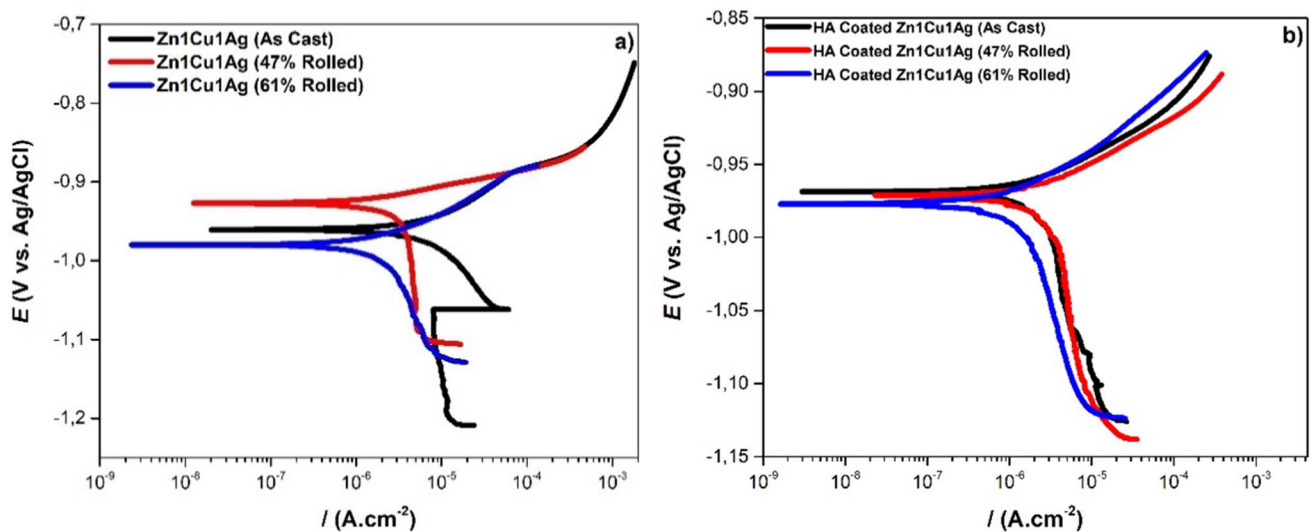


Fig. 9 PDS curves of **a** as-cast, 47% and 61% rolled, **b** HA coated as-cast, 47% and 61% rolled

c, J_{corr}) computed from the Tafel extrapolation method are shown in Table 2.

SBF is one of the multi-complex ion containing solutions used in corrosion analysis of possible biomedical implants, and the order of the ion complexity in the mediums is reported as NaCl < Phosphate-buffered saline (PBS) < Ringer's solution < Simulated body fluid

(SBF) < Minimum essential medium (MEM) < Fetal bovine serum (FBS) or bovine serum albumin (BSA) [44]. When specimens were immersed into the solution, dissolution of alloying metals started to be expected according to Eqs. 1, 2 and 3, because the corrosion rendering media consists serious amount of ions including some aggressive ones, such as chloride ions.

Table 2 Calculated corrosion parameters of uncoated and coated ZnCu1Ag samples

	ID	E_{corr} (mV)	I_{corr} (μA)	β_a (V dec. ⁻¹)	β_c (V dec. ⁻¹)	J_{corr} ($\mu\text{A cm}^{-2}$)
Uncoated	As-cast	-961	10.5	0.0857	0.1744	214.3
	47% rolled	-927	1.4	0.0236	0.052	35
	61% rolled	-980	3.28	0.0684	0.5416	93.7
HA coated	As-cast-HA	-969	2.35	0.036	0.1786	61.8
	47% rolled-HA	-971	2.66	0.0338	0.2197	56.6
	61% rolled-HA	-977	1.35	0.0421	0.1867	26.5



PDS results can be divided into several regions. From the PDS curves of uncoated samples, given in Fig. 9a, it can be seen that As-cast and 47% rolled samples revealed parallel cathodic curves to the potential axis from -1.2 to -1.05 V, and -1.1 to -0.95 V, respectively. Parallel progress of the curve to the potential axis in the cathodic region means the current density is limited by the oxygen consumption reaction, given in Eq. 4(b), leading by the dissolved oxygen in the aqueous NaCl solution. Then, hydrogen generation reaction, given in Eq. 5, is started to dominate for both as-cast and 47% rolled samples from -1.05 to -0.97 V and -0.95 to -0.92 V, respectively. The reason behind this claim is emerging from both their standard reduction potentials [45] and the kinetic investigation via hydrodynamic electro-analytical techniques [46, 47]. When the table of standard reduction potentials is investigated, it can be seen that the oxygen consumption reaction requires less electromotor force than the hydrogen reduction (0 V for $2\text{H}^+ + 2e^- \rightarrow \text{H}_{2(\text{g})}$, and 0.4 V for $\text{O}_2 + 2\text{H}_2\text{O} \rightarrow 4\text{OH}^-$, at 25 °C in water), and therefore electronegative surface more aggressively attracts the dissolved oxygen in aerated NaCl solution [48, 49]. Detailed investigations for electrode kinetics and mechanisms by creating a well-defined laminar flow profile throughout the surface via rotating disc electrode reveal that the main reduction reaction is driven in case of the existence of dissolved oxygen [47]. In other words, at higher overpotentials, the diffusion of oxygen to the electroactive area limits the current density, resulting in the current-potential curve proceeding parallel to the potential axis. Then, the parallel current-potential curve eventually evolves into a slope dominating the hydrogen generation, given in reaction 5 [50]. However, the parallel current-potential curve can also initiate a slope without revealing the limiting current density of dissolved oxygen diffusion as seen in the %61 rolled sample due to various factors, such as variation of dissolved oxygen level, and surface properties.

Analyzing the cathodic portions of PDS curves for samples coated with HA, limiting the current density of dissolved oxygen is not come insight, both hydrogen generation and oxygen consumption are expected to be present (Fig. 9b). The anodic part of uncoated samples slightly differs from each other with expected anodic dissolution reactions. All three uncoated samples portray acceleration in corrosion at around -0.9 V, but until this potential, the speed of the corrosion rate (slope of the curves vs current axis) for the samples can be written as 61% rolled < as-cast < 47% rolled. When the anodic region of HA-coated samples was investigated, the rate of corrosion was found slower for all three when compared to the uncoated samples because the slope of the anodic curves increased by revealing decreasing rate of current increase.

While the various ions are exist in the SBF solution, the main medium is water-based, and therefore; the corrosion zones/products of the tested samples will be formed metal oxides or hydroxides according to the given reactions in Eqs. 6 and 7 [51].



Evaluating the potentiodynamic scanning data shown in Fig. 9, it is evident that the as-cast sample's curve has a clear change in the cathodic direction. The reason for the formation of the curve in this way can be explained by the rapid formation non-uniform zones by oxidation products which is expected in multi-ion containing solutions as discussed before. In Fig. 9a, the cathodic curve of the as-cast sample and %47 rolled sample ends up with higher E_{corr} values than the %61 rolled sample, but the rapid climb of the potential curve of the as-cast sample in the anodic direction reveals a higher slope resulting in relatively higher J_{corr} value than the %47 rolled sample. While the %47 rolled sample is also expected to reveal higher J_{corr} with higher I_{corr} at first view from its emerged higher E_{corr} value, the slow increase of

potential curve with lower slope led it to have resulted in relatively lower I_{corr} and J_{corr} values. For the HA-coated samples, given in Fig. 9b, emerging slopes are not several times higher than each other, as in uncoated samples. However, a relatively lower cathodic slope and E_{corr} of %61 rolled sample resulted in lower I_{corr} and J_{corr} values when compared to the as-cast and %47 rolled sample.

In comparison to the as-cast sample, lower I_{corr} values (1.4 and $3.28 \mu\text{A cm}^{-2}$, respectively) and J_{corr} values (35 and $93.7 \mu\text{A cm}^{-2}$, respectively) were found when 47% and 61% of the rolled samples were investigated. The 47% and 61% rolled samples showed worse corrosion resistance and a rise in I_{corr} value from 1.4 to $3.28 \mu\text{A cm}^{-2}$ upon independent analysis. While the secondary phases act as the anode in alloying with metals with lower electrode potential than Zn, the secondary phases act as a cathode in alloying with metals with higher electrode potential than Zn, and therefore the corrosion rate increases [52–54]. In some cases, the secondary phases formed can be broken by the effect of plastic deformation and form a granular structure via dynamic

recrystallization resulting in a decrease passive film density (see I_{corr} in Table 2 and Figs. 2 and 10) [55]. This could potentially be an additional factor contributing to the rise in corrosion rate as the rolling rate increases [56].

Upon analyzing the HA-coated samples using the EPD method, the as-cast sample's I_{corr} value decreased from 10.5 to $2.35 \mu\text{A cm}^{-2}$, and the J_{corr} value decreased from 214.3 to $61.8 \mu\text{A cm}^{-2}$. In the 61% sample, the I_{corr} value decreased from 3.28 to $1.35 \mu\text{A cm}^{-2}$, while the J_{corr} value decreased from 93.7 to $26.5 \mu\text{A cm}^{-2}$. This situation concluded that HA coating on these samples had a positive effect on corrosion resistance. The presence of a porous form of HA deposition, as shown in Fig. 11, can lead to this consequence. It is anticipated that the porous structure reduces the number of corrosion sites on the surface by potentially creating a Cassie-Baxter state [57]. The cassie-Baxter state claims that low surface tension liquids, such as hexane (0.013 mN m^{-1}), can reach the nanoholes in a porous structure, but in the case of relatively higher surface tension liquids, such as water (73 mN m^{-1}) or SBF ($\approx 64 \text{ mN m}^{-1}$), possible air-filled dry

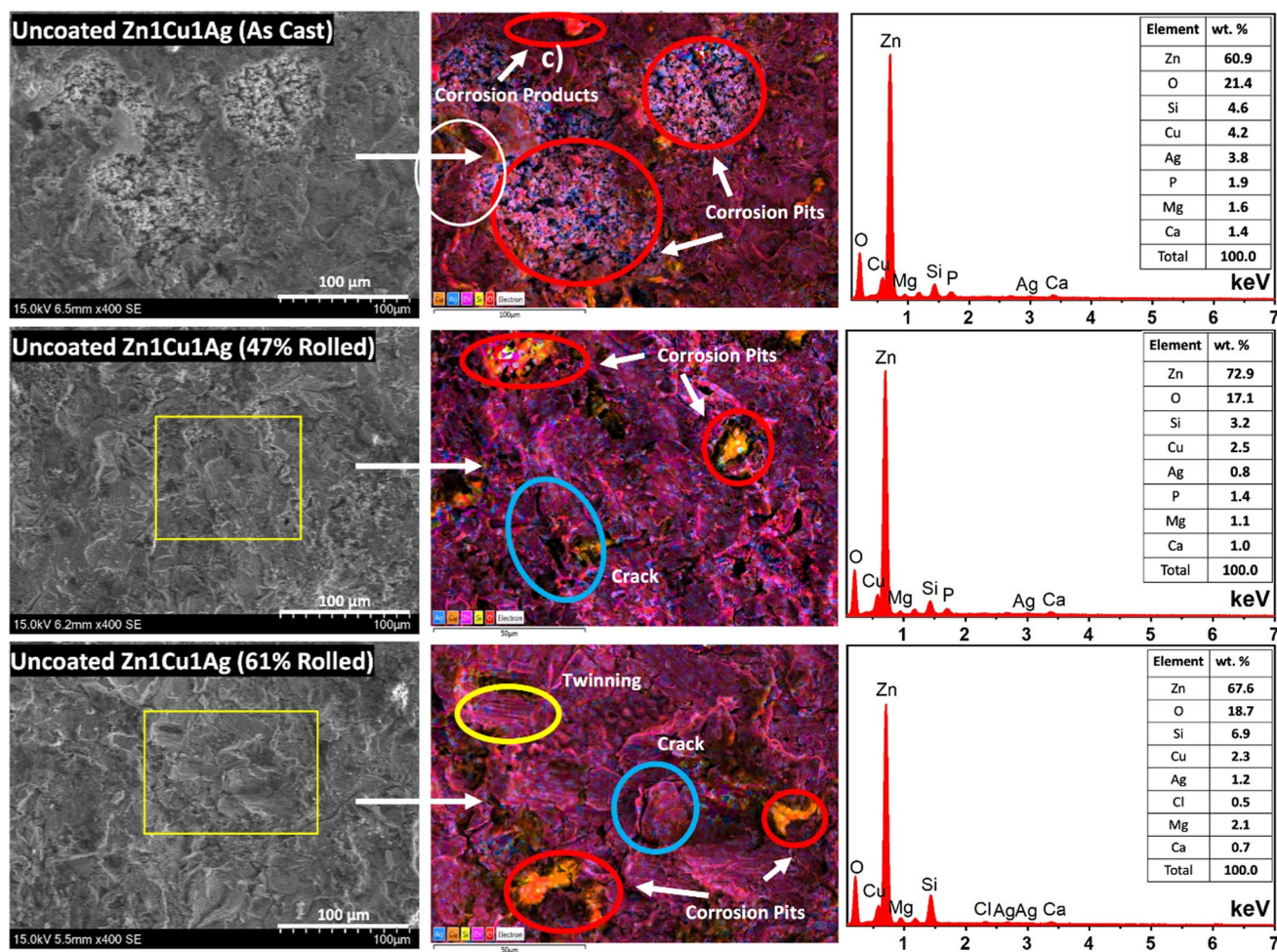


Fig. 10 SEM images and EDS-mapping analysis of a uncoated as-cast, b 47%, and c 61% rolled Zn1Cu1Ag samples, after corrosion

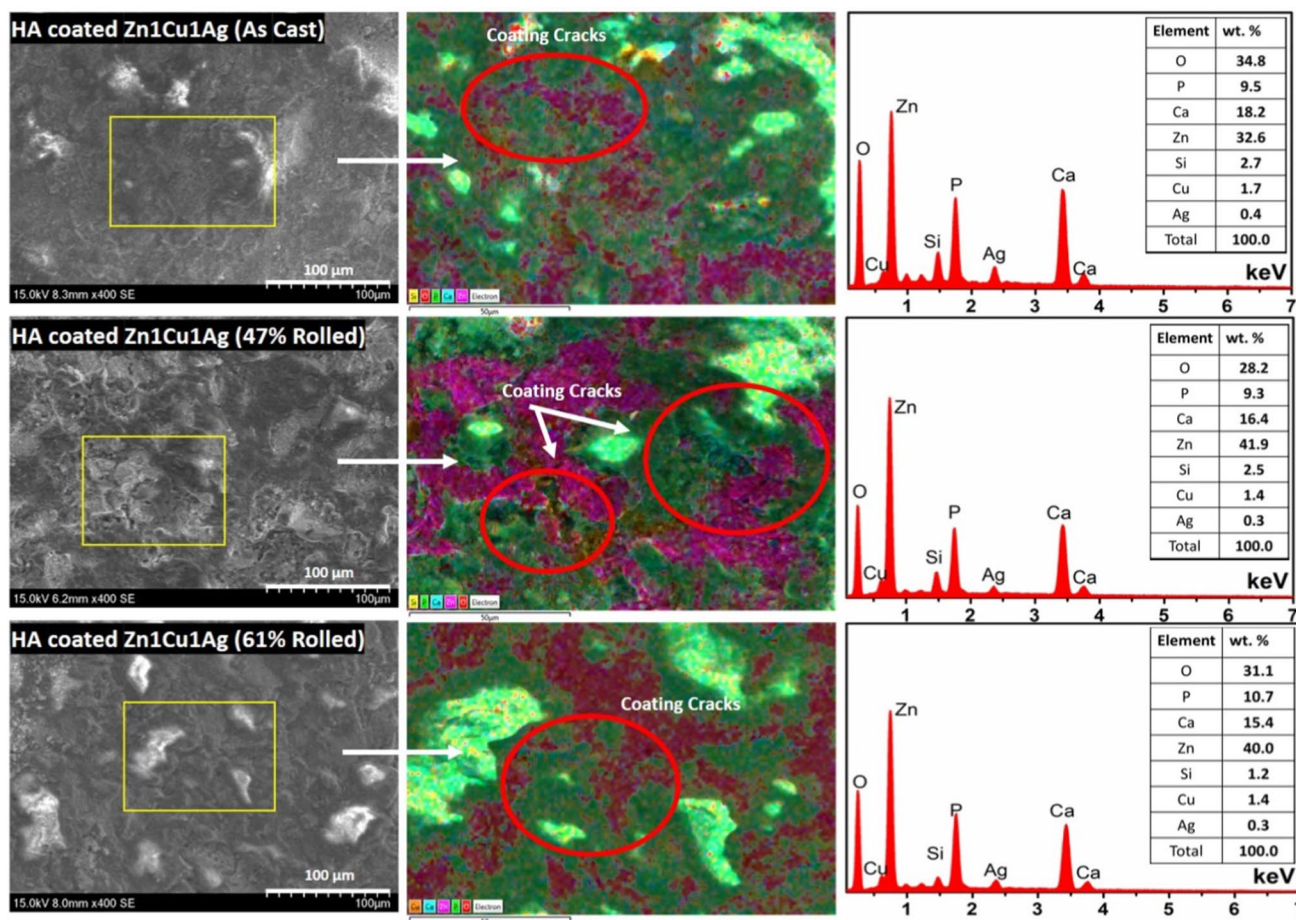


Fig. 11 SEM images and EDS-mapping analysis of **a** HA coated as-cast, **b** 47%, and **c** 61% rolled samples after corrosion

surfaces in the porosity can be either inaccessible or become slowly accessible [50]. Hence, it may be inferred that the presence of porosity on the surface of liquids with increased surface tension may lead to a decreased progression of galvanic cells at corrosion sites.

In the 47% rolled sample, the I_{corr} value after coating increased from $1.4 \mu\text{A}$ to $2.66 \mu\text{A cm}^{-2}$ and also the J_{corr} value increased from 35 to $56.6 \mu\text{A cm}^{-2}$. In addition, post-coating corrosion resistance increased, however the expected improvement was not observed. This may be due to a lower coating adhesion and wettability of the 47% rolled samples.

3.6 SEM–EDS Analyzes of Corroded Surfaces

SEM–EDS examinations of uncoated-cast, but 47% and 61% rolled Zn1Cu1Ag samples were performed to assess surface properties following corrosion tests (Fig. 10). Analysis of Fig. 10 suggests that corrosion is prevalent in specific locations and that its impact causes abrasions on the material's surface. The shift in the cathodic direction in the Tafel curve of the as-cast sample can be explained as the reduction of

corrosion resistance with the formation of these large pits with corrosion products in the image. An examination of the colored elemental distribution map shows that Zn, Cu, and Ag elements are plentiful in locations where pit formation occurs. At the same time, while the corrosion products were not evenly dispersed, they were spread across the corrosion pits.

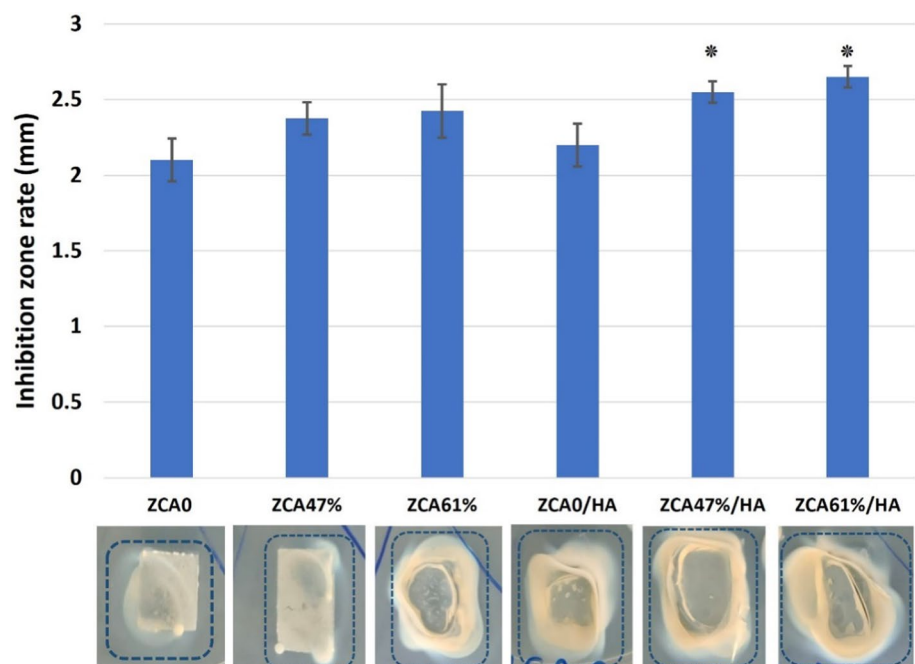
The rolled samples' surfaces exhibit a distinct corrosion behavior in contrast to the cast sample. Corrosion in the casting sample is localized in specific locations, however in the rolling samples, it is more evenly distributed across the surface and exhibits lower intensity than anticipated. It can be concluded that the corrosion resistance of the as-cast sample is significantly lower than that of the rolled samples by examining the post-corrosion SEM pictures of as-cast, 47%, and 61% rolled samples.

SEM–EDS evaluations of HA coated as-cast, 47%, and 61% rolled Zn1Cu1Ag samples were done to analyze the surface features after the corrosion test and identify the corrosion products created, as shown in Fig. 11. The rolled samples, unlike the as-cast sample, exhibit no evidence of

pitting corrosion, and the corrosion products appear to be very tiny and distributed throughout the surface. The presence of yellow-weighted images was detected when the EDS images were examined. Although these photographs were initially thought to depict corrosion pits, the color mapping method revealed that they were rich in Si and O, indicating casting holes. It has been demonstrated that the resulting products are consistent with previous studies [58, 59]. Furthermore, because the corrosion products formed generally contain O, it is possible to interpret the corrosion rate with the amount of O found in the EDS analysis after corrosion. The PDS curves indicated that the fastest corroding sample was the as-cast one.

While the samples showed no significant pitting, the EDS analysis revealed that the corrosion products were equally distributed across the entire surface. Furthermore, white structures are visible in some areas of the coated surfaces. Ca, P, and O elements, which are frequently seen in the HA structure, were detected in the regions corresponding to these structures during the EDS investigation (Fig. 11). The reason for the formation of such bright regions is interpreted as the formation of coatings is more intense and the coating thickness increases compared to other regions. Furthermore, it is found that novel corrosion products are created as a result of the corrosion test performed in SBF, as anticipated and mentioned in the corrosion section. The existence of a high oxygen-O content in the coated hydroxyapatite (HA) structure does not always result in more intense corrosion products, as demonstrated by comparing uncoated energy-dispersive spectroscopy (EDS) values obtained after corrosion.

Fig. 12 Histogram of inhibition zone diameters obtained after antibiotic susceptibility test against *E. coli* incubation, * $p < 0.05$



3.7 Antibacterial Analysis

The antibacterial efficiency of a Zn–Cu–Ag alloy was tested against *E. coli* after being manufactured, rolled, and coated with hydroxyapatite (HA) on Zn1Cu1Ag samples. The bacteria were grown in a medium containing Zn1Cu1Ag alloy. On *E. coli*, the inhibition rates of the ZCA EPD groups were higher than those of the ZCA Base groups. In the *E. coli* incubation, the average inhibition rate was 26.5 mm in ZCA61% -HA, 25.5 mm in ZCA47% -HA, 22 mm in ZCA0 -HA, 24.25 mm in ZCA61 Base, 23.75 mm in ZCA47% Base, and 21 mm in ZCA0 Base (Fig. 12). Because of their high surface area, Ag may physically connect with the cell surface of bacteria, allowing for improved interaction. Furthermore, Ag may induce damage to bacterial cell membranes, increasing bacterial membrane permeability, and it is most likely to impact the bacterial respiratory chain [60, 61]. As a result, the combinations of Zn–Cu and Ag suppressed bacteria and shown a high antibacterial activity as given in Fig. 12.

3.8 Cell Viability Analysis

The effect of ZCA alloys on L929 cell viability was evaluated by MTT assay. According to ISO 10993–5:2009, a cytotoxic effect emerges when cell viability is decreased to 70% in the control group [34]. As cell viability was found good in all materials at 24 h, however, they decreased below 70% in some samples after 72 h. Despite a decrease in viability in all groups at 48 h, the HA coated samples did not induce toxicity at 48 h. The cell viability

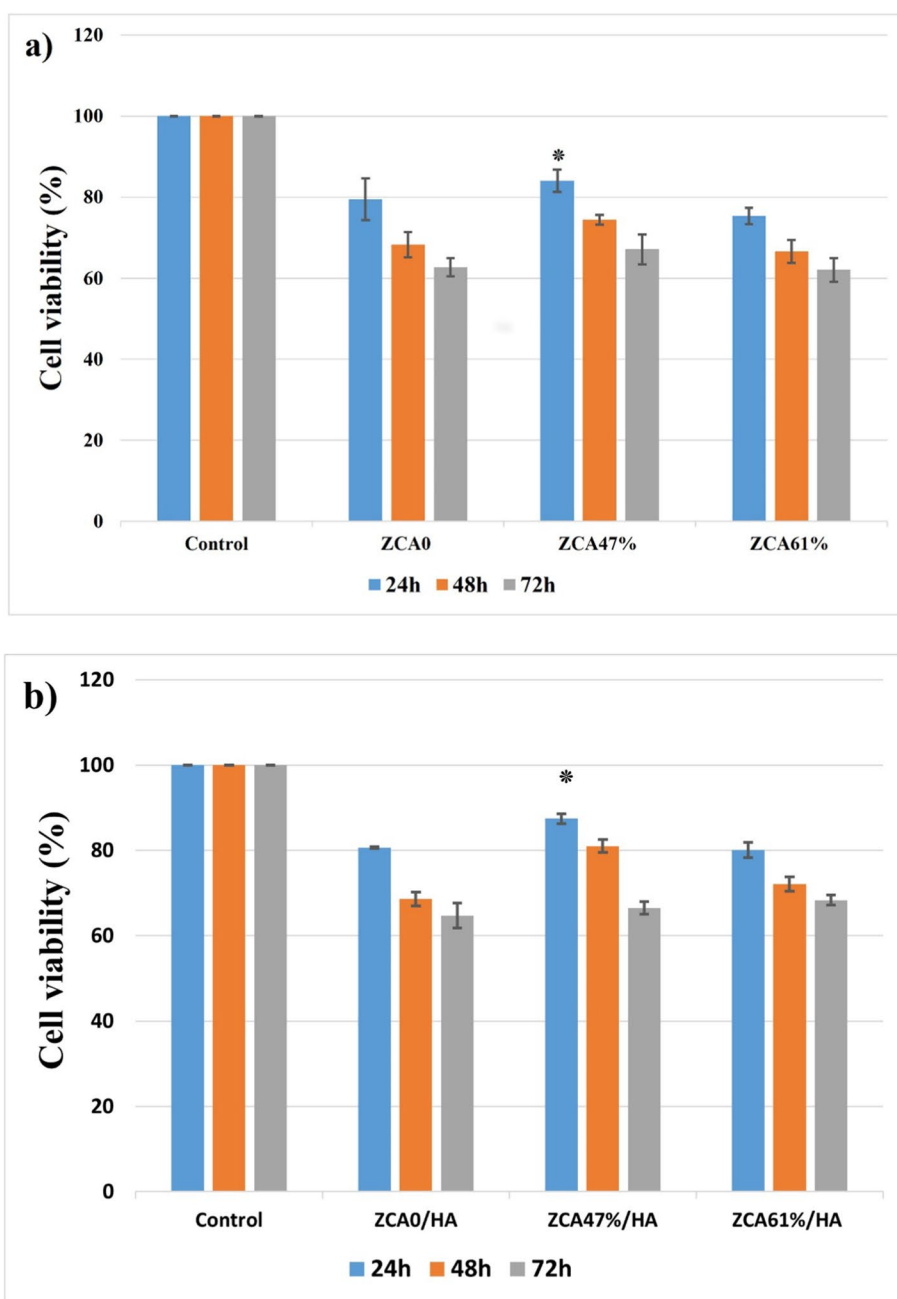
rates were assessed in the ZCA61%/HA group (61% deformed and HA coated), the ZCA47%/HA group (47% deformed and HA coated), the ZCA0/HA group (undeformed-HA coated), the ZCA61% base group (75.39% deformed—uncoated), the ZCA47% base group (84.01% deformed—uncoated), and the ZCA0 base group (undeformed—uncoated) after a 24-h period. Such rates in different groups after 48 h were determined as: 73.13% in ZCA61%/HA, 81.01% in ZCA47% -HA, 70.58% in ZCA0 -HA, 66.64% in ZCA61% base, 74.45% in ZCA47% base, and 68.27% in ZCA0 base (Fig. 13a,b). The ZCA47%—HA alloys demonstrated a significant enhancement in cell

viability, with an observed increase of around 4%–8% over a period of 24 and 48 h (Fig. 14).

4 Conclusions

The objective of this study was to examine the effects of two distinct deformation rates (47% and 61%) on the Zn–1Cu–1Ag alloy, which was fabricated by the arc casting technique. In addition, an analysis was conducted to examine the impact of hydroxyapatite coatings on Zn1C–u1Ag surfaces, with a focus on comparing the corrosion

Fig. 13 The effects of cell viability of **a** uncoated ZCA0, ZCA47%, ZCA61%, **b** HA-coated; ZCA0, ZCA47%, ZCA61% on L929 for 24, 48 and 72 h. * $p < 0.05$



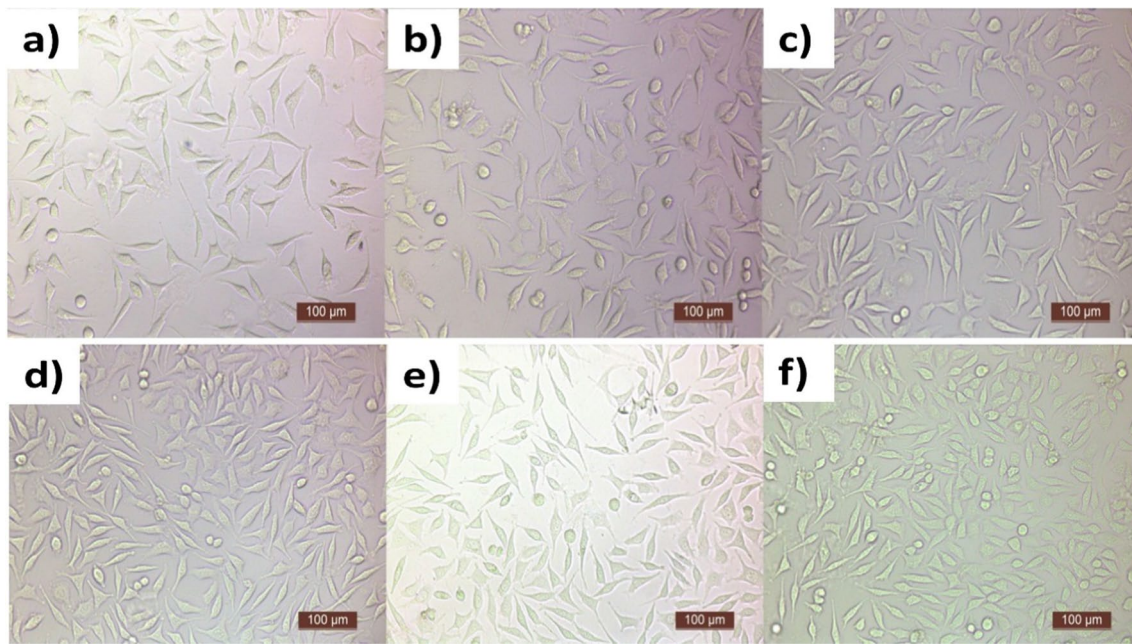


Fig. 14 Inverted microscope images of materials applied L929 fibroblast cells at 24 h. **a** ZCA0, **b** ZCA47%, **c** ZCA61%, **d** ZCA0-HA, **e** ZCA47%-HA, **f** ZCA61%-HA

resistance patterns exhibited by the sample surfaces. Microstructure studies revealed that the secondary (Ag, Cu)Zn4 phase formed and that its concentration increased with increasing rolling rate. The grains elongated along the rolling direction, and the secondary phase formed along the rolling direction, resulting in a fine-grained structure. As the rolling rate increased, the mechanical properties of the Zn–1Cu–1Ag alloy improved. The maximum values obtained were 88.10.5 HV hardness and 412.65 MPa compression strength in 61% of the rolled samples. Except for the %47 rolled HA coated sample, the corrosion resistance of HA coated Zn1Cu1Ag samples revealed better results when compared to uncoated ones. Possible cracks on the electroactive corrosion area of 47% rolled sample are expected to be the main cause of the decrease in corrosion resistance. The corrosion tests revealed that the HA-coated 61% rolled sample performed the best, with values of 1.35 mA I_{corr} and 26.5 mA $\text{cm}^{-2} J_{\text{corr}}$ values. In general, it can be concluded that the increase in the deformation rate resulted in an increment of inhibition zones and the abundance of inhibition zones in ZCA61% is expected, and thus resulted in better corrosion resistance. Furthermore, for the 47% rolling rate, ZCA samples revealed the maximum cell viability for both coated and uncoated samples. Therefore, a 47% rolling rate with HA coating is the most feasible sample for sought corrosion resistance and cell viability.

Author Contributions B. A: Project administration, Methodology, Writing—original draft, Validation. E. I: Experimental work, graphical presentation of the results. N. A: Characterization analysis, Writing & editing. S.C: Corrosion tests and writing. S.S: Deformation–rolling process.

Funding Open access funding provided by the Scientific and Technological Research Council of Türkiye (TÜBİTAK). The authors declare that no funds, grants, or other support were received during the preparation of this manuscript.

Data Availability The data and code that support the findings of this study are available from the corresponding author upon reasonable request.

Code Availability Not applicable.

Declarations

Conflict of interest The authors declare that they have no potential competing interests that could interfere with his/her full capacity of being perfectly objective regarding his/her research and manuscript.

Ethical Approval The work is original and has not been published previously or is not under consideration for publication elsewhere. If accepted, it will not be published elsewhere in any form without a copyright holder.

Consent to Participate All authors have read and agreed to the submitted version of the manuscript. Informed consent was obtained from all individual participants included in the study.

Consent for Publication Not applicable in this manuscript.

Open Access This article is licensed under a Creative Commons Attribution 4.0 International License, which permits use, sharing, adaptation, distribution and reproduction in any medium or format, as long as you give appropriate credit to the original author(s) and the source, provide a link to the Creative Commons licence, and indicate if changes were made. The images or other third party material in this article are included in the article's Creative Commons licence, unless indicated otherwise in a credit line to the material. If material is not included in the article's Creative Commons licence and your intended use is not permitted by statutory regulation or exceeds the permitted use, you will need to obtain permission directly from the copyright holder. To view a copy of this licence, visit <http://creativecommons.org/licenses/by/4.0/>.

References

- B.M. Holzapfel, J.C. Reichert, J.-T. Schantz, U. Gbureck, L. Rackwitz, U. Nöth, F. Jakob, M. Rudert, J. Groll, D.W. Hutmacher, *Adv. Drug Deliv. Rev.* **65**, 581 (2013)
- Y.F. Zheng, X.N. Gu, F. Witte, *Mater. Sci. Eng. R Reports* **77**, 1 (2014)
- Z.O. Králová, R. Gorejová, R. Oriňáková, M. Petráková, A. Oriňák, M. Kupková, M. Hrubovčáková, T. Sopčák, M. Baláž, I. Maskaľová, A. Kovalčíková, K. Koval', *Prog. Nat. Sci. Mater. Int.* **31**, 279 (2021)
- F. Witte, N. Hort, C. Vogt, S. Cohen, K.U. Kainer, R. Willumeit, F. Feyerabend, *Curr. Opin. Solid State Mater. Sci.* **12**, 63 (2008)
- Z. Sheikh, S. Najeeb, Z. Khurshid, V. Verma, H. Rashid, M. Glogauer, *Materials (Basel)* **8**, 5744 (2015)
- P.K. Bowen, E.R. Shearier, S. Zhao, R.J. Guillory, F. Zhao, J. Goldman, J.W. Drelich, *Adv. Healthc. Mater.* **5**, 1121 (2016)
- K.M. Hambidge, N.F. Krebs, *J. Nutr.* **137**, 1101 (2007)
- P.K. Bowen, R.J. Guillory, E.R. Shearier, J.-M. Seitz, J. Drelich, M. Bocks, F. Zhao, J. Goldman, *Mater. Sci. Eng. C* **56**, 467 (2015)
- H. Yang, B. Jia, Z. Zhang, X. Qu, G. Li, W. Lin, D. Zhu, K. Dai, Y. Zheng, *Nat. Commun.* **11**, 401 (2020)
- P. Li, W. Zhang, J. Dai, A.B. Xepapadeas, E. Schweizer, D. Alexander, L. Scheideler, C. Zhou, H. Zhang, G. Wan, J. Geis-Gerstorf, *Mater. Sci. Eng. C* **103**, 109826 (2019)
- W. Bednarczyk, M. Wątroba, J. Kawałko, P. Bała, *Mater. Sci. Eng. A* **748**, 357 (2019)
- Z. Tang, J. Niu, H. Huang, H. Zhang, J. Pei, J. Ou, G. Yuan, *J. Mech. Behav. Biomed. Mater.* **72**, 182 (2017)
- J. Niu, Z. Tang, H. Huang, J. Pei, H. Zhang, G. Yuan, W. Ding, *Mater. Sci. Eng. C* **69**, 407 (2016)
- L. Li, C. Liu, H. Jiao, L. Yang, F. Cao, X. Wang, J. Cui, *J. Alloys Compd.* **888**, 161529 (2021)
- M. Sikora-Jasinska, E. Mostaed, A. Mostaed, R. Beanland, D. Mantovani, M. Vedani, *Mater. Sci. Eng. C* **77**, 1170 (2017)
- P. Li, C. Schille, E. Schweizer, F. Rupp, A. Heiss, C. Legner, U.E. Klotz, J.G. Gerstorfer, L. Scheideler, *Int. J. Mol. Sci.* **19**, 755 (2018)
- H. Kabir, K. Munir, C. Wen, Y. Li, *Bioact. Mater.* **6**, 836 (2021)
- M.E. Aksoy, B. Aksakal, N. Aslan, B. Dikici, *J. Mater. Eng. Perform.* **30**, 7365 (2021)
- Y. Bi, W. Xiong, Z. Li, K. Wang, L. Liu, X. Yin, D. Sun, H. Li, Y. Song, W. Li, S. Yu, *Met. Mater. Int.* **30**, 667 (2024)
- R.T. Candidato, P. Sokołowski, L. Pawłowski, G. Lecomte-Nana, C. Constantinescu, A. Denoirjean, *Surf. Coat. Tech.* **318**, 39 (2017)
- B. Dikici, M. Niinomi, M. Topuz, Y. Say, B. Aksakal, H. Yilmazer, M. Nakai, *Prot. Met. Phys. Chem. Surf.* **54**, 457 (2018)
- B. Aksakal, M. Gavgali, B. Dikici, *J. Mater. Eng. Perform.* **19**, 894 (2010)
- B. Aksakal, Y. Say, Z.A. Sinirlioglu, *Mater. Today Commun.* **33**, 104246 (2022)
- D. Liu, K. Savino, M.Z. Yates, *Surf. Coat. Tech.* **205**, 3975 (2011)
- Z. Chunyan, M. Yanlong, L. Chenglong, *Prot. Met. Phys. Chem. Surf.* **55**, 127 (2019)
- M.E. Aksoy, B. Aksakal, N. Aslan, B. Dikici, *Prot. Met. Phys. Chem. Surf.* **57**, 1040 (2021)
- X. Sun, S. Tang, Y. Zhou, Y. Mao, J. Hu, W. Wang, J. Han, *Met. Mater. Int.* **29**, 2571 (2023)
- E. Mohseni, E. Zalnezhad, A.R. Bushroa, *Int. J. Adhes. Adhes.* **48**, 238 (2014)
- X. Meng, T.-Y. Kwon, Y. Yang, J.L. Ong, K.-H. Kim, *J. Biomed. Mater. Res. Part B Appl. Biomater.* **78B**, 373 (2006)
- V. Hybasek, J. Kubasek, J. Capek, D. Alferi, J. Pinc, J. Jiru, J. Fojt, *Corros. Sci.* **187**, 109520 (2021)
- A. Oyane, H.-M. Kim, T. Furuya, T. Kokubo, T. Miyazaki, T. Nakamura, *J. Biomed. Mater. Res. A* **65**, 188 (2003)
- R. Humphries, A.M. Bobenchik, J.A. Hindler, A.N. Schuetz, *J. Clin. Microbiol.* **59**, 00213-21 (2021)
- M. Balouiri, M. Sadiki, S.K. Ibsouda, *J. Pharm. Anal.* **6**, 71 (2016)
- Biological evaluation of medical devices Part 5: Tests for in vitro cytotoxicity, ISO 10993-5 (ISO, Geneva, 2009)
- E. Kilicay, E. Erdal, B. Hazer, M. Türk, E.B. Denkbaz, *Artif. Cells Nanomed. Biotechnol.* **44**, 1938 (2016)
- Z.-Z. Shi, X.-X. Gao, H.-J. Zhang, X.-F. Liu, H.-Y. Li, C. Zhou, Y.-X. Yin, L.-N. Wang, *Bioact. Mater.* **5**, 210 (2020)
- H. Baker, H. Okamoto, *ASM Handbook. Vol. 3: Alloy Phase Diagrams* (ASM International, Materials Park, 1992), p. 501
- T. Di, Y. Xu, D. Liu, X. Sun, *Metals (Basel)* **12**, 1444 (2022)
- E. Mostaed, M.S. Ardakani, M. Sikora-Jasinska, J.W. Drelich, *Mater. Lett.* **244**, 203 (2019)
- A. Jarzębska, M. Bieda, J. Kawałko, Ł. Rogal, P. Koprowski, K. Sztwiertnia, W. Pachla, M. Kulczyk, *Mater. Lett.* **211**, 58 (2018)
- C. Chen, R. Yue, J. Zhang, H. Huang, J. Niu, G. Yuan, *Mater. Sci. Eng. C* **116**, 111172 (2020)
- J. Jiang, H. Huang, J. Niu, Z. Jin, M. Dargusch, G. Yuan, *Scr. Mater.* **200**, 113907 (2021)
- E.C. Donaldson, W. Alam, *Wettability* (Elsevier, Netherlands, 2013)
- D. Mei, S.V. Lamaka, X. Lu, M.L. Zheludkevich, *Corros. Sci.* **171**, 108722 (2020)
- Y. Liu, T. Du, A. Qiao, Y. Mu, H. Yang, *J. Funct. Biomater.* **13**, 164 (2022)
- A.R. Kucernak, C. Zalitis, *J. Phys. Chem. C* **120**, 10721 (2016)
- M.C. van Ede, U. Angst, *Corros. Eng. Sci. Technol.* **59**, 39 (2024)
- M. Nie, J.A. Wharton, A. Cranny, N.R. Harris, R.J.K. Wood, K.R. Stokes, *Materials (Basel)* **6**, 4345 (2013)
- J. Jung, S. Oh, H. Kwon, *Mater. Corros.* **72**, 557 (2021)
- S. Cihangir, *Turkish J. Nature Sci.* **12**, 15 (2023)
- S. Cihangir, *Adv. Eng. Mater.* **25**, 2300731 (2023)
- J. Huang, Y. Lai, H. Jin, H. Guo, F. Ai, Q. Xing, X. Yang, D.J. Ross, *J. Mater. Eng. Perform.* **29**, 6484 (2020)
- H. Yilmazer, S. Basit, A. Sen, Y. Yilmazer, B. Dalbayrak, E.D. Arisan, S. Arisan, R.K. Islamgaliev, B. Dikici, *J. Alloys Compd.* **965**, 171290 (2023)
- R.E. Hammam, S.A. Abdel-Gawad, M.E. Moussa, M. Shoeib, S. El-Hadad, *Int. J. Met.* **17**, 2794 (2023)
- Z. Jia, B. Yu, L. Fu, *Materials (Basel)* **15**, 6343 (2022)
- C. García-Mintegui, L.C. Córdoba, J. Buxadera-Palmero, A. Marquina, E. Jiménez-Piqué, M.-P. Ginebra, J.L. Cortina, M. Pegueroles, *Bioact. Mater.* **6**, 4430 (2021)
- B.M.L. Koch, A. Amirfazli, J.A.W. Elliott, *J. Phys. Chem. C* **118**, 23777 (2014)
- E. Mostaed, M. Sikora-Jasinska, A. Mostaed, S. Loffredo, A.G. Demir, B. Previtali, D. Mantovani, R. Beanland, M. Vedani, *J. Mech. Behav. Biomed. Mater.* **60**, 581 (2016)
- D. Palai, T. Roy, P.S. Prasad, C. Hazra, S. Dhara, R. Sen, S. Das, K. Das, *A.C.S. Biomater. Sci. Eng.* **8**, 1443 (2022)
- G. Franci, A. Falanga, S. Galdiero, L. Palomba, M. Rai, G. Morelli, M. Galdiero, *Molecules* **20**, 8856 (2015)
- X. Hong, J. Wen, X. Xiong, Y. Hu, *Environ. Sci. Pollut. Res.* **23**, 4489 (2016)

Publisher's Note Springer Nature remains neutral with regard to jurisdictional claims in published maps and institutional affiliations.